Journal of Wind Engineering & Industrial Aerodynamics 250 (2024) 105760

Contents lists available at ScienceDirect

Journal of Wind Engineering & Industrial Aerodynamics

journal homepage: www.elsevier.com/locate/jweia

Design and demonstration of a sensing network for full-scale wind pressure measurements on buildings

John Hochschild *, Catherine Gorlé

Stanford University, Y2E2 Building, 473 Via Ortega, Stanford, CA, 94305, United States of America

ARTICLE INFO

Keywords:
Full-scale measurements
Non-Gaussian wind pressures

ABSTRACT

There is a need for full-scale wind pressure measurements to evaluate the accuracy of peak wind load estimates from wind tunnel measurements, numerical simulations, or building codes. The objective of this study was to design a sensing network for obtaining long-term records of fluctuating wind pressures, and to demonstrate the network's potential through deployment. A custom data-logger using the BMP388 absolute pressure sensor, which can measure pressure coefficients within ±0.1 at a wind speed of 10 m/s, was designed. The accuracy of the measured statistics was established through comparison with a standard differential sensor in a wind tunnel experiment. A network of 10 motes was deployed on the sloped roof of the 184 m tall Space Needle, obtaining over 1000 h of fluctuating pressure data. The measurements reveal a windward separation region with strong dependency of the approach wind turbulence on the pressure statistics, but positive skewness limits the peak values. The skewness becomes negative near the edge of a second, leeward separation region, resulting in peak factors up to 2.6 times larger than the code-prescribed value of 3.4. The results demonstrate that long-term full-scale measurements provide valuable insight into peak wind pressures and their dependence on approach wind characteristics.

1. Introduction

As more and more of the world's population lives in dense cities, the need to accurately characterize wind loads experienced by high-rise buildings is greater than ever. One only needs to read the news to see examples of high-rises experiencing wind effects that negatively impact their design integrity. In March 2023, failure of glass cladding panels on a San Francisco office building during a wind event sent the neighborhood into lockdown to prevent pedestrians being hit by falling glass. In New York City, the highly-slender 432 Park Avenue provides an example of a building that is reportedly uninhabitable due to uncomfortable displacements during high winds: residents complain of creaking, plumbing issues, and elevator malfunctions (Chen, 2021).

Currently, wind loads on buildings are estimated either using building codes and standards, which are based on empirical information from wind tunnel pressure measurements on canonical building shapes, or using dedicated wind tunnel measurements for the specific building under consideration. There are two important limitations to this approach. First, it is assumed that peak pressures measured on small-scale wind tunnel models are representative of those experienced by full-scale buildings. Previous studies comparing wind loads measured at model- and full-scale on low-rise structures have consistently found peak pressures to be underestimated at model-scale (Richardson and Surry, 1991; Richardson et al., 1997; Okada and Ha, 1992; Cochran and Cermak, 1992; Ho et al., 2003; Liu et al., 2009). The discrepancies are attributed to differences in the approach turbulent wind fields as well as to suppression of the smaller turbulent scales at lower Reynolds numbers (Re) (Richardson et al., 1997; Hagos et al., 2014; Okada and Ha, 1992; Tieleman, 2003; Morrison et al., 2013). Both approach flow and Re effects can be expected to also occur on high-rise buildings; however, there is presently a lack of full-scale data for high-rises.

Most of the data used for investigating statistical treatment of peak pressures are sourced from wind tunnel measurements and full-scale measurements of low-rise buildings (Wacker et al., 1991; Peng et al., 2014; Liu et al., 2017; Subramanian et al., 2012; Sridhar et al., 2021). Two exceptions are data from full-scale measurements on a 45-story rectangular office building in Montreal (Dalgliesh, 1971) and on a 57-story building in Toronto (Dalgliesh et al., 1980). However, both of these experiments used differential sensors and so obtained wind pressure coefficients highly influenced by the building's dynamic internal pressure.

The objective of this study is to design and demonstrate a wireless sensor network for recording long-term full-scale wind pressure measurements on high-rise buildings. The time period of the measurements should be sufficiently long to obtain independent measurements over

* Corresponding author.
E-mail addresses: john.hochschild@us.af.mil (J. Hochschild), gorle@stanford.edu (C. Gorlé).

https://doi.org/10.1016/j.jweia.2024.105760
Received 3 August 2023; Received in revised form 12 April 2024; Accepted 1 May 2024
Available online 10 May 2024

a range of atmospheric wind conditions. The network uses absolute pressure sensors to obtain measurements that are independent of internal pressurization and support comparison with wind tunnel or numerical simulation results. A suitable sensor was identified through testing in a small wind tunnel and subsequently validated in a large atmospheric boundary layer wind tunnel. A network of wireless data-logging "motes" that features the absolute sensor was then designed and fabricated. To demonstrate the sensor network's capabilities, the network was installed on the Space Needle for several months. The pressure measurements were post-processed to obtain the statistical moments of fluctuation pressure coefficient C_p' and the corresponding peak gust factor. The resulting values are compared with those from building codes to evaluate code accuracy and potentially identify any shortcomings. In the future, the data can be used to make direct comparisons with wind tunnel experiments and computational simulations, supporting quantitative validation of these methods.

Section 2 explains the need for a custom datalogger and details the resulting design and validation testing. Section 3 describes the Space Needle deployments, and Section 4 presents and discusses the results of the full-scale experiment. Conclusions are presented in Section 5.

2. Sensor selection and testing of a pressure-sensing mote

2.1. Quantities of interest

In experiments and simulations of wind loading, the quantities of interest are the statistics of the pressure coefficients C_p on the building surfaces:

$$C_p(t) = \frac{P(t) - \overline{P}_{ref}}{\frac{1}{2}\rho\overline{U}^2} \tag{1}$$

where $P(t)$ is the time series of the absolute pressure measured on a building, $\overline{P}_{ref}$ is the time-averaged reference pressure, ρ is the density, and $\overline{U}$ is the time-averaged windspeed at building height. The key statistics calculated from each time series are the mean, standard deviation, peak value, skewness, and kurtosis.

When using differential sensors, $\overline{P}_{ref}$ is the reference end of the sensor. When using absolute sensors, a second sensor is necessary to measure the barometric reference $\overline{P}_{ref}$. In either instance, obtaining a stable and appropriate measure of $\overline{P}_{ref}$ in full-scale experiments is a difficult task (Dalgliesh, 1971; Dalgliesh et al., 1980) that can introduce significant uncertainty in the values of $C_p(t)$. While this uncertainty will directly affect the mean value of the time series, the statistics of the fluctuating pressure coefficient can be recovered with high accuracy. Considering that the turbulent statistics are also considered the more difficult quantities to predict accurately, both in scaled wind tunnel experiments (Richardson et al., 1997; Cochran and Cermak, 1992; Okada and Ha, 1992; Liu et al., 2009) and in CFD simulations (Ricci et al., 2017, 2018; Cao et al., 2019), we therefore define our quantities of interest for the full scale measurements as the statistics of the fluctuating pressure coefficient C_p':

$$C_p'(t) = \frac{P(t) - \overline{P}}{\frac{1}{2}\rho\overline{U}^2} \tag{2}$$

where $\overline{P}$ is the time-average of $P(t)$. The specific statistics of interest are the second, third, and fourth moments of $C_p'(t)$, i.e. the root-mean-square (rms), kurtosis, and skewness respectively. The rms value will be denoted as $C_{p,rms}$, since $C'_{p,rms} = C_{p,rms}$. In addition, we will consider the minimum peak value $C'_{p,min}$ and the peak factor g, which is the ratio of $C'_{p,min}$ to $C_{p,rms}$.

The calculation of these statistics from full scale measurements introduces additional challenges due to the variability in the natural wind. The mean wind speed and direction can vary considerably within the length of time that is typically used for sampling in wind tunnel experiments (often at least 2 h full-scale equivalent (Kasperski, 2003; Pomaranzi et al., 2022)). When considering shorter time periods, internal variability in the turbulent flow can result in significant differences in the turbulent statistics for the same mean wind speed and wind direction. To understand and quantify these effects, one of the main requirements for our sensor network is that it should support long term measurements of the fluctuating pressure coefficients, such that a large number of independent shorter (10-min) time series can be obtained to quantify these effects. The calculation methods to obtain the fluctuation statistics from these time series are detailed in Section 3.3.

2.2. Sensor network requirements

The goal is to support deployment of a network of about 20 sensors on buildings for a period of several months. The sensors should be able to make repeatable C_p' measurements even in relatively low winds so that we may gather many independent time series. These objectives necessitate unique requirements for the sensor and network design: low-noise sensing at a sufficiently high temporal frequency in a compact and unobtrusive housing.

First, the pressure sensor used must have low-noise and be able to measure small changes. To support measurements in relatively low wind conditions, we specified that the pressure coefficient uncertainty ΔC_p should not exceed 0.1 at windspeed $U = 10$ m/s, so the sensor uncertainty must not exceed 6 Pa. Furthermore, a resolution in C_p of 0.005 or lower was desired, meaning required sensor resolution was 0.3 Pa or lower. Wind tunnel measurements typically measure pressure at tap locations with frequency $\mathcal{O}(500-1000$ Hz), assuming 1:100 scale this is equivalent to $\mathcal{O}(10$ Hz) at full-scale.

The objective necessitated further requirements for the sensor's data logger, which together with the sensor comprise a mote in the network. Because each is fixed to the exterior of a large building, access is difficult so they must be solar-powered and record data wirelessly. They also must be as unobtrusive as possible, to prevent influencing the flow and mitigate building owners/operators' concerns on their aesthetic impact. Finally, they must of course be weatherproof.

No commercially available solutions meeting the requirements were known so a custom mote was designed and manufactured for the experiment. The characteristics of the sensor used and the design details of the data-logging mote are described in the next subsection.

2.3. Sensor selection and validation

The selection and validation of the pressure sensor was performed in two steps. Initial tests of several high-resolution pressure sensors were performed in Stanford's small-scale teaching wind tunnel to determine the sensors' capability to measure accurate pressure coefficient fluctuation statistics. Next, we performed further validation of the selected sensor during an experiment performed in a larger scale atmospheric boundary layer (ABL) wind tunnel. This section summarizes the set-up and results of these tests.

2.3.1. Initial sensor selection and validation in small-scale wind tunnel

Fig. 1(a) shows a diagram of the tests performed in Stanford's small scale teaching wind tunnel. A 20 cm cube was placed in the 76 cm x 76 cm test section and exposed to a uniform, low turbulence, incoming velocity profile. Several candidate absolute sensors were embedded in the top surface, along with a differential sensor as a baseline. Rectangular cutouts were etched into the cube surface so that the sensors would be flush with the face. The sensors were arranged along a line perpendicular to the incoming flow and as close together as practical to ensure they see similar flow conditions. A low-profile vented enclosure installed upstream of the cube housed an additional absolute sensor and the reference port of the differential sensor, both to measure reference pressure.

The test was divided into regions of approximately constant freestream velocity ($\Delta U < 0.12$ m/s) and at each U the pressure

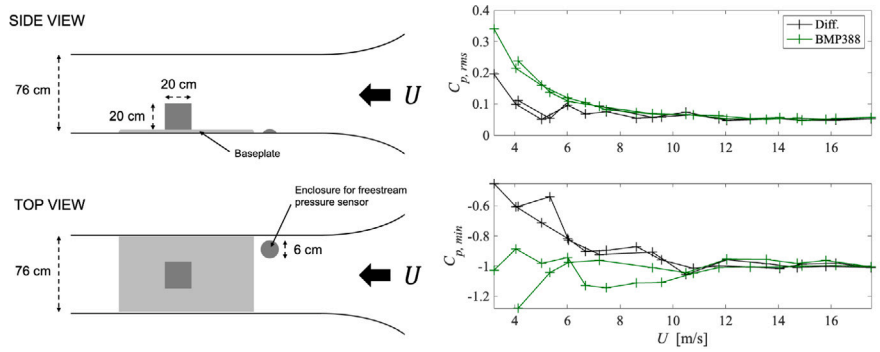

(a) Diagram of wind tunnel test setup.

(b) $C_{p,rms}$ and $C_{p,min}$ measured by BMP388 and differential sensor as a function of freestream velocity .

Fig. 1. Schematic and results of initial wind tunnel test for sensor selection.

coefficient was calculated for each sensor. RMS and minimum C_p were calculated as a function of U and compared between the different sensors. Fig. 1(b) shows the comparison between the differential sensor and the Bosch Sensortec BMP388 sensor, which we found to be the most optimal. The BMP388 is a MEMS (micro-electromechanical systems) sensor with very small footprint and a built-in 24-bit analog-to-digital converter (Bosch Sensortec, 2018). For ease of use, we use sensors pre-installed on breakout boards, which are 2 cm square in dimension. The results show that with 1.7 Pa RMS noise, the sensor's signal-to-noise ratio is sufficiently high to make meaningful C_p measurements when $U > 10$ m/s. The $C_{p,rms}$ plot indicates that sensor noise dominates at low wind speeds. However, given constant sensor noise, the noise contribution to $C_{p,rms}$ decreases proportionally to U^2, and accurate measurements of the turbulent fluctuations are obtained at velocities exceeding 10 m/s.

Finally, although sensor drift is not a driving concern because it only affects the mean and not the turbulent measure C_p', a long-term test over several weeks showed the maximum half-span of the drift to be 5.5 Pa, which corresponds to $\Delta C_p = 0.09$ when $U = 10$ m/s. The sensor measures at 12.5 Hz and has 0.17 Pa resolution, exceeding both requirements identified in the previous section.

The next subsection details a validation of the BMP388 against differential sensors nominally used in experiments at an atmospheric boundary layer wind tunnel facility.

2.3.2. Sensor validation in ABL wind tunnel test

During a series of tests at the Florida International University's Wall of Wind, an open section wind tunnel with a 6.1 m wide and 4.3 m high test section, two pressure taps on a scale model of a low-rise building were each simultaneously connected to a standard differential sensor (Scanivalve ZOC33) and to a BMP388. The barometric reference pressure was measured with a third absolute sensor. The building model, shown in Fig. 2, was a 1:100 model of Stanford's Y2E2 building, measuring 1 m long, 0.64 m wide, and 0.21 m high. The model was tested for a suburban terrain exposure at 36 wind directions spanning the full range $[0, 360]°$. 117 s (1468 samples at 12.5 Hz) of time series was obtained for each wind direction and from each a peak value was estimated using the statistical method introduced in Cook and Mayne (1979, 1980), which is explained in more detail in Section 3.3.2. Fig. 2 includes the model orientation and the locations of the two pressure taps on the North facade and South facades. Inflow profiles and other details of this experiment are available from Vargiemezis and Gorlé (2024).

C_p statistics from the test are plotted as a function of wind direction in Fig. 3. Although the root-mean-squared difference, annotated on the plots, is below 0.1 for all statistics, we observe a noticeable bias for tap 418: $C_{p,mean}$ is higher for the absolute sensor than the differential sensor at all wind directions. This bias is attributed to the difficulty of measuring a valid reference pressure, and will not affect our main goal of measuring C_p' statistics.

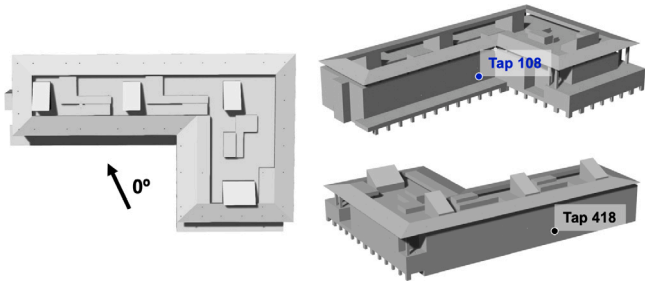

Fig. 2. Three views of the Y2E2 building, indicating the tap positions on the facade.

The spectra are compared in Fig. 4 and the distributions of C_p' are compared in Fig. 5. Although the distributions shown in Fig. 5 are very similar, we see that the absolute sensors measure fewer data points with C_p' very close to 0, which can be attributed to these sensors' higher noise. To illustrate this, $\pm C_p'$ corresponding to $\Delta P = 1.7$ Pa is shown on the plots by dashed lines.

2.4. Mote design

2.4.1. Sensor waterproofing

The BMP388 sensor is not inherently waterproof so a system was designed to prevent water reaching the sensor during rain. Fig. 6 shows the design. Hydrophobic acoustic mesh (not pictured but denoted by a dashed line) prevents most water from entering the tubing system. The small amount of water that does pass through preferentially flows down through the Y-connector away from the sensor and collects in a capped reservoir. An additional layer of acoustic mesh between the Y-connector and the sensor further prevents water from reaching the sensor. Any water that collects in the reservoir will gradually evaporate out.

The wind tunnel setup introduced in Section 2.3.1 and shown in Fig. 1 was used to ensure the waterproofing system was not affecting sensing dynamics. The inflow port of the waterproofed sensor and a fully-exposed sensor were installed in the top face of the cube. A time series portion and spectrum for both waterproofed and the exposed sensors are compared in Fig. 7. The excellent agreement between the results confirms that the waterproofing system does not affect the sensor dynamics.

2.4.2. System and electronics design

Traditional environmental sensing networks require two types of components: motes with sensors and base station(s) that receive data

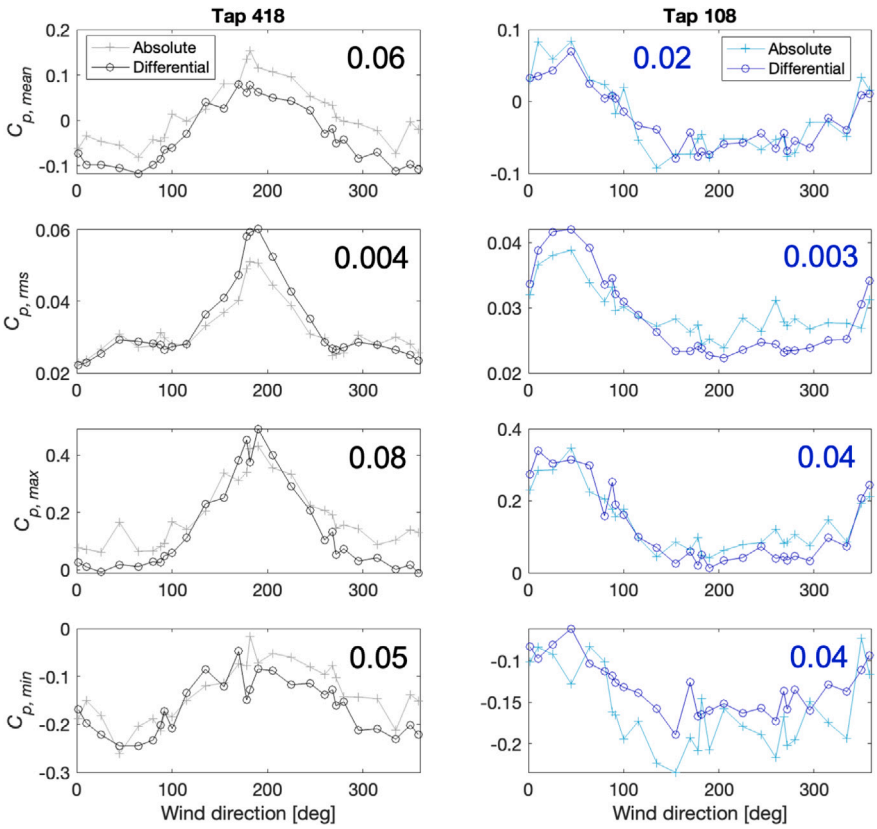

Fig. 3. Comparison of C_p statistics for both differential and absolute sensors as a function of wind angle. Root-mean-squared difference is annotated in black/blue.

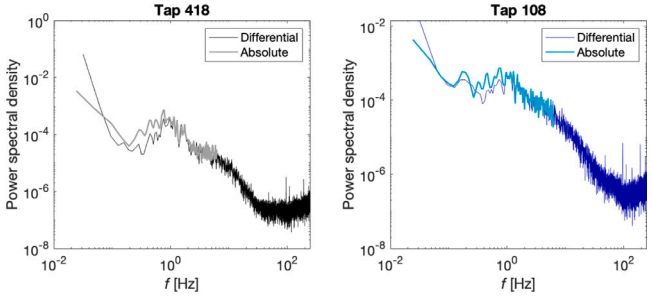

Fig. 4. Comparison of spectra for both differential and absolute sensors, at 1.8° wind direction. The differential sensor data has not been filtered here.

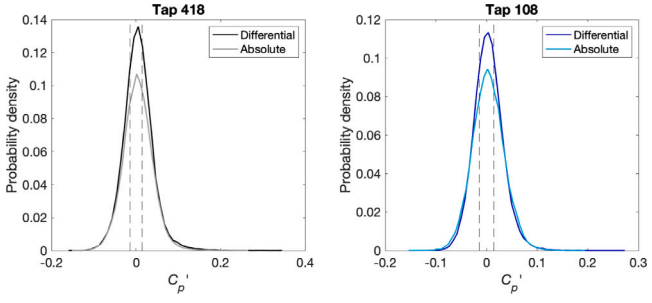

Fig. 5. Comparison of fluctuating component of pressure coefficient C_p' for both differential and absolute sensors. The dashed lines, denoting the range of sensor noise contribution, are at $C_p' = \frac{1.7\ \text{Pa}}{0.5\rho U^2} = 0.028$.

from motes and upload it to the cloud (Liao et al., 2014; Subramanian et al., 2011). For our network we instead use Wifi or cellular enabled

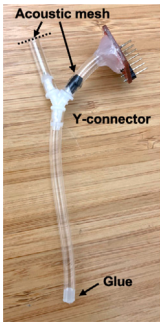

Fig. 6. Sensor waterproofing system.

Arduino microcontrollers on each mote. Power consumption analysis showed that a Wifi-enabled Arduino board uses comparable power as a Zigbee RF transceiver, which is commonly used to send data to base stations in the traditional network architecture. Using internet-enabled Arduinos in each mote removes the need for base-stations and eliminates associated range concerns. Measurements are logged directly to an Amazon Web Services database using the MQTT protocol.

While Wifi-connected motes use the Arduino Nano 33 IoT or MKR 1010, cellular-connected motes use the Arduino MKR 1500 NB. Both varieties can go into a low-power deep sleep mode, which is used when windspeed is low. When in sleep mode, they connect to the internet every 20 min to check the windspeed. If it meets a threshold value, the mote awakens and starts acquiring data.

Initial deployments of cellular- and Wifi- connected motes on the Space Needle failed to gather significant amounts of data because of high RF noise at the top of the building. The Wifi router we installed measured the noise to be as high as −55 dBm: a level so high that even motes a few meters away could not connect to the network. Because

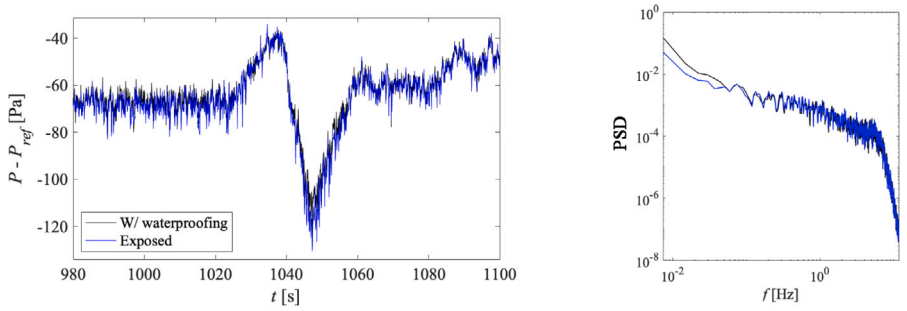

(a) Pressure time series showing response to large increase/decrease in freestream velocity.

(b) Spectra for the period of the test with $U > 5$ m/s.

Fig. 7. Waterproofing wind tunnel test results.

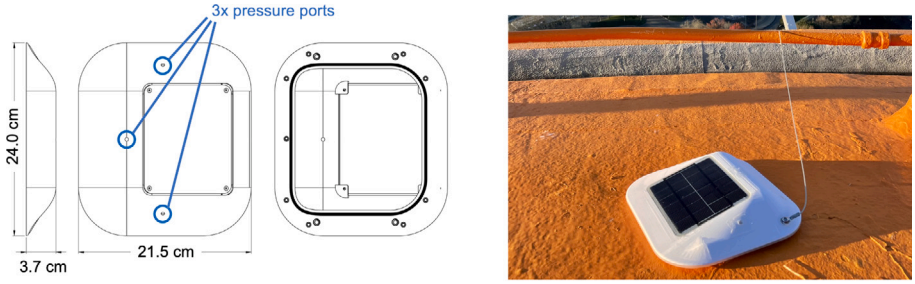

(a) Three-view schematic of mote housing.

(b) Mote mounted on the Space Needle roof.

Fig. 8. Mote housing.

of this, we later retrofitted the motes to be disconnected and log data to SD cards. Instead of checking the windspeed, every 20 min the SD motes check P_{rms} measured by the onboard sensors and only wake if $P_{rms} > 10$ Pa, where this threshold value was chosen based on analysis of previous measurements.

A 2 W solar panel was chosen to power the mote, which allows for several hours of acquisition per day, but the exact number highly depends on climate and orientation. In addition to power components, a DS3231 high-precision real time clock (RTC) is used in the mote to provide greater time precision than is possible with only an Arduino. Testing showed that the use of the precision RTC allows for synchronization between motes with an offset of less than 0.1 s.

2.4.3. Housing design

The housing was designed to accommodate the solar panel, three sensors, and other electronics. A schematic is shown in Fig. 8(a) and a photo of a mounted mote is shown in Fig. 8(b). The housing is 3D printed in white to minimize solar heating. It was designed to be as compact as possible to minimize aerodynamic influence on the pressure measurements. Since it can be expected that aerodynamic effects will occur under certain flow conditions, the three sensors incorporated on different faces of each mote are used to exclude data whenever the three sensors measure significantly different statistics. Section 3.3 further describes how our post-processing routine checks for data outliers due to possible aerodynamic influence from the mote geometry.

3. Space needle experimental setup and post-processing methods

The first building on which we deployed the absolute pressure sensor network was the Space Needle, a 184 m tall observation tower in Seattle, Washington. The building is just north of Downtown Seattle, about 700 m inland from Elliot Bay. There are no other tall buildings in the immediate vicinity, which will simplify future efforts towards comparison with wind tunnel or CFD models.

To measure C_p', the pressure P on the building was measured by the motes and U was determined from anemometer measurements. The details of these are given in the following subsections. The data is accessible on Mendeley at https://data.mendeley.com/datasets/8pxgdp7cn7/3.

3.1. Anemometers

Three ultrasonic anemometers were installed to characterize the wind incident on the building. Two were installed on the roof of the Pacific Science Center (PacSci), a mid-rise building that is about 150 m upstream of the Space Needle for the dominant wind direction. The PacSci anemometers were installed primarily to aid future comparisons to CFD simulations. Photographs of the installed anemometers are shown in Fig. 11(a)–(c).

Calculation of C_p' requires knowledge of the freestream velocity at building height. The wind speed measured by the anemometer installed at the top of the Space Needle has to be corrected to account for the influence of the building geometry. We determined this correction factor by performing a large-eddy simulation that showed a 32% acceleration of the flow measured at this position relative to freestream velocity at building height. Therefore, measurements from this anemometer are used in the calculation of C_p' but with a 0.76 correction factor multiplied.

3.2. Mote placements

Table 1 summarizes the four deployments on the Space Needle's roof. The motes were placed around the perimeter of the sloped roof (see Fig. 9), about 30 cm from the edge. Due to connectivity issues and water ingress, not all sensors gathered data. Specifically, electromagnetic noise on the building meant that connecting to either Wifi or cellular networks was often difficult. Furthermore, given the exposure of the building and the typical wet conditions in Seattle, rain penetrated a few sensors through either the housing seal or the hydrophobic mesh. (December 2022 and January 2023 were especially wet, even by

Table 1
Number of sensor-hours of time series data obtained per deployment, with the mote technology used for each.

Deployment	Technology	Sensor-hours of data
May–Jul 2022	Cellular motes	282
Nov–Dec 2022	Wifi motes	0
Dec 2022–Jan 2023	SD motes	145
Feb 2023	SD motes	608
		1035

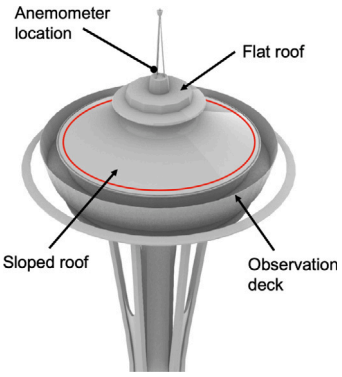

Fig. 9. Space Needle, with sloped roof perimeter indicated in red.

Seattle's standards, which explains the lower amount of data for this period.) Future iterations of the mote housing will have more robust sealing to minimize water ingress. Ultimately, data was successfully gathered at the 10 distinct positions shown in Fig. 10.

3.3. Post-processing methods

The measured wind velocity and fluctuating pressure time series are divided into 10-min periods during which the mean wind speed and wind direction can be considered constant. These time series are used directly to calculate wind velocity and pressure statistics. In addition, we calculate statistics over ensembles of 10-min time series to characterize the effect of the approach wind turbulence intensities and to calculate minimum peak pressure coefficients using longer cumulative time records. Because of the circular shape of the building, the fluctuating pressure statistics will be presented as a function of the angle along the perimeter of the roof, where the 0° point is defined as the most upstream point on the roof given the mean wind direction during the specific measurement period. The following sections introduce the equations and calculation methods used.

3.3.1. Turbulent wind statistics from anemometer data

From the anemometer time series, we calculate the streamwise turbulence intensity $I_u = \sigma_u/\overline{U}$, as well as the streamwise integral time scale T_u. σ_u is the standard deviation of the streamwise velocity time series and $\overline{U}$ the mean streamwise velocity. T_u is computed by integrating the autocorrelation of $U(t)$. Taylor's hypothesis can then be used to approximate integral length scale:

$$L_{u,x} \approx T_u U \tag{3}$$

Past studies have shown a dependency of wind pressure fluctuation statistics on both the turbulence intensity and the length scale (e.g. Saathoff and Melbourne, 1997; Lamberti and Gorlé, 2020; Yang et al., 2022a). To investigate this relationship based on our full-scale measurements we also define the turbulence parameter η as follows (Saathoff and Melbourne, 1997):

$$\eta = I_u \left(L_{u,x}/D\right)^{0.15}, \tag{4}$$

where $D = 37.2$ m is the roof diameter.

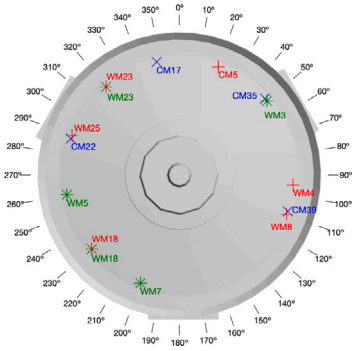

Fig. 10. Positions of motes that gathered data. Blue corresponds to the cellular mote deployment, green to the first SD mote deployment, and red to the second.

As mentioned in Section 3.1, the rooftop anemometer does not provide a freestream measurement. In the current analysis, we therefore assume that the turbulence intensities and length scales measured by the rooftop anemometer are representative of those in the freestream. The relationships between these quantities in the freestream and at the rooftop anemometer will be estimated using large-eddy-simulations in future work. We also note that the anemometer measurements support calculation of spanwise turbulence intensities and length scales. These spanwise statistics are not used or reported in this paper, but they will be used to inform future computational modeling efforts.

3.3.2. Calculation of statistics over 10-min periods

The 10-min time series are used directly to calculate the rms, skewness, kurtosis, and spectra. The minimum peak fluctuation values $C'_{p,min}$ are obtained from an extreme value analysis. The time series of C'_p is divided into 16 windows, and the peak value from each window is recorded. Assuming a type I (Gumbel) extreme value distribution for the peak samples, the peak values with a non-exceedance probability of 78% are then given by $m + 0.636\sigma$, where m and σ are the mean and the rms value of the 16 peak values (Cook and Mayne, 1979, 1980). When dividing the 10-min sampling time into 16 windows, the length of each window is less than the minimum window length $T_{target} = 10$ min suggested by Cook and Mayne. The values are therefore corrected to account for the actual sampling time T_{actual} as follows (Kasperski, 2003):

$$C'_{p,min} = m + \left(0.636 + \frac{\sqrt{6}}{\pi} ln \frac{T_{target}}{T_{actual}}\right) \sigma \frac{m}{|m|} \tag{5}$$

We calculate the peak factor g, as defined in Eq. (6).

$$g = \frac{C_{p,peak} - C_{p,mean}}{C_{p,rms}} = \frac{C'_{p,peak}}{C_{p,rms}} \tag{6}$$

The resulting values will be interpreted by comparing them to the constant value of 3.4 prescribed by the North American building code, ASCE 7-22 (American Society of Civil Engineers, 2022).

The reported values for these statistics will be affected by uncertainties introduced by the relatively short sampling window used for their estimation. These effects will be more important for higher order statistics and for the peak fluctuation and peak factor estimates. The calculation of $C'_{p,min}$ includes the correction factor for the sampling time (Eq. (5)), which is equal to 2.2 when using 10-min time series, but uncertainty associated with this correction factor remains (Kasperski, 2003).

Lastly, to account for the possibility that the mote shape influences the pressure measurements, our post-processing routine checks for differences between the values measured at the three pressure ports, each positioned on different faces. For any given 10-min window, if the range between $C_{p,rms}$ measurements exceeds 0.04 or if the range

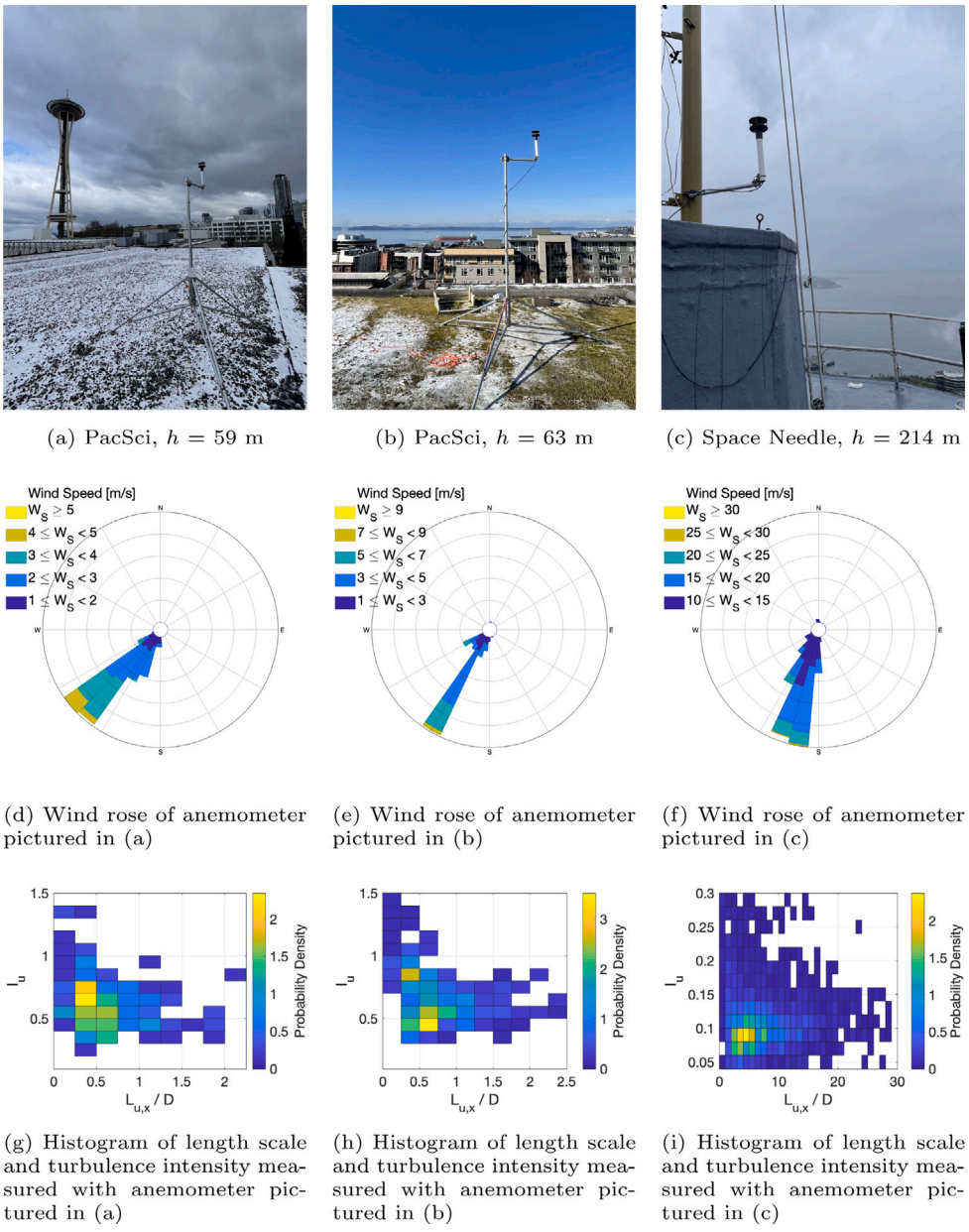

(a) PacSci, $h = 59$ m (b) PacSci, $h = 63$ m (c) Space Needle, $h = 214$ m

(d) Wind rose of anemometer pictured in (a) (e) Wind rose of anemometer pictured in (b) (f) Wind rose of anemometer pictured in (c)

(g) Histogram of length scale and turbulence intensity measured with anemometer pictured in (a) (h) Histogram of length scale and turbulence intensity measured with anemometer pictured in (b) (i) Histogram of length scale and turbulence intensity measured with anemometer pictured in (c)

Fig. 11. Summary of anemometer placement and measurements.

between $C'_{p,min}$ measurements on a single mote exceeds 0.4, this 10-min window is excluded for all sensors. The choice of these threshold values represents a trade-off between retaining data and excluding suspected outliers and could be adjusted based on the requirements of specific experiments.

3.3.3. Ensemble post-processing

During the analysis, we observed significant variation in the turbulent wind statistics between different 10-min sampling periods, as well as a correlation between these velocity statistics and $C_{p,rms}$ and $C'_{p,min}$. To analyze this effect, we group the measurements in ensembles with similar turbulence intensities and position along the perimeter within a 10° sector. For $C_{p,rms}$, we then calculate the mean and 1.96σ confidence interval over all 10-min time periods in each of these groups. For $C'_{p,min}$, we calculate the values from an extreme value analysis performed over all the 10-min time series available within the group. This calculation follows the process outlined in Section 3.3.2, but since it employs at least 16 10-min windows the correction term expressed as a function of T_{target}/T_{actual} in Eq. (5) reduces to 0. Spectra will also be ensemble averaged over the groups. We note that the calculation of statistics over ensembles of 10-min time series offers one way to reduce the uncertainty related to convergence of the statistical estimation process, provided that the underlying distributions of the 10-min windows are the same.

4. Space needle results

4.1. Windspeed

Wind roses and histograms of 10-min mean turbulence intensities and length scales are shown in Fig. 11. We are only plotting measurements during acquisition periods, i.e. when the rooftop anemometer 10-min mean exceeded 10 m/s. Note that the results from the PacSci anemometers are not used here but will be used for comparison and validation of CFD simulations.

Fig. 11(f) shows how acquisition was largely at the dominant wind direction as measured at the top of the building: for 87% of the 10-min measurement periods the wind direction is between 180° and 220°.

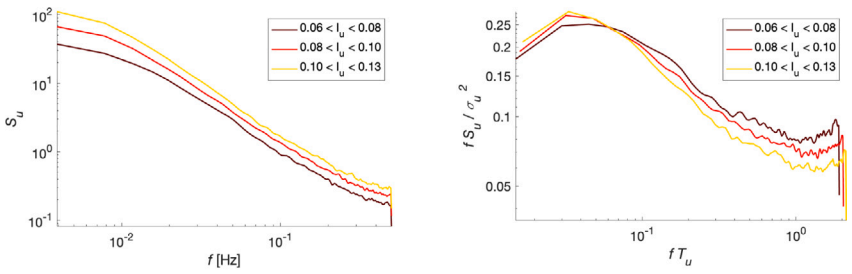

(a) Dimensional. (b) Normalized.

Fig. 12. Spectra of the turbulent wind velocity measured by the rooftop anemometer, binned by turbulence intensity.

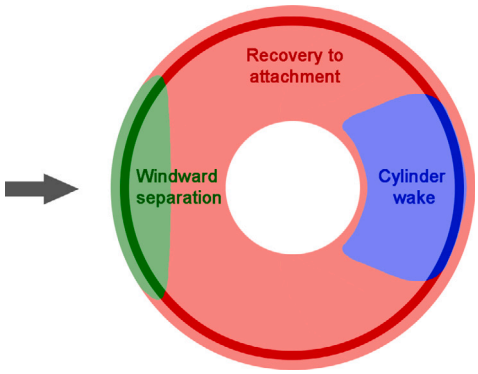

Fig. 13. Possible shapes of the windward and leeward separation regions. The arrow denotes wind direction.

Fig. 11(i) shows a joint histogram of the streamwise turbulence intensities and length scales measured at the same location. I_u varies from around 5% to 15%, with a few measurement periods showing slightly higher or lower values. The length scales $L_{u,x}$ non-dimensionalized by roof diameter predominantly lie within the range $2 < L_{u,x}/D < 8$. To explain the reason for the variability in the turbulent wind statistics, we explored correlations between the turbulence intensity and the mean wind speed, mean wind direction, temperature, and Richardson number at roof height, but all correlations were found to be negligible.

Fig. 12 shows the dimensional (a) and normalized (b) spectra of the measured wind velocity. Individual spectra were calculated for each 10-min period, followed by grouping them in 3 turbulence intensity bins and then ensemble averaging. The dimensional plot indicates an overall increase in fluctuation across all scales, with the strongest increase at the largest scales. The normalized spectra further show that during periods with higher turbulence intensity there is comparatively more energy content at the larger scales in the flow.

The effect of the variability in turbulence intensity on the measured pressure time series is analyzed in the following sections.

4.2. $C_{p,rms}$ and $C'_{p,min}$

To support the presentation and discussion of the fluctuation pressure coefficient statistics, it is useful to first consider the flow pattern expected on the Space Needle's sloped roof. Overall, we expect to see three key flow regions, as illustrated in Fig. 13, with the perimeter band emphasized to show where we measured C'_p. First, there is a windward separation region, caused by the flow separating over the vertical glazed panels mounted around the observation deck below, as illustrated in Fig. 9. This flow separation happens before the flow reaches the roof edge. Second, there is a region aft of this separation, where the flow recovers to attached flow. Last, there is the cylinder wake region behind the central raised roof section.

$C_{p,rms}$ and $C'_{p,min}$ around the perimeter of the roof are shown in Fig. 14. Each data point corresponds to statistics calculated from a 10-min time series. For $C'_{p,min}$, the 10-min is subdivided into 16 intervals and the extreme value analysis described in Section 3.3 is performed using the 16 intervals. The plot shows symmetrical behavior, as expected given the geometrical symmetry. The highest $C_{p,rms}$ values occur around 0° (or 360°) in the windward separation region (see Fig. 13). $C_{p,rms}$ then gradually decreases across the attached flow region until the values increase again in the shear layer between the attached flow and the cylinder wake. In the cylinder wake, the $C_{p,rms}$ values decrease again. $C'_{p,min}$ shows the same trend, but with opposite sign. The data points are colored by the turbulence intensity measured at the rooftop anemometer, indicating a correlation between the turbulence intensity and the intensity of the pressure fluctuations.

Fig. 15 further visualizes these trends by calculating the fluctuating pressure statistics using ensembles, grouping the data points by position (in 10° increments) and by turbulence intensity. For $C_{p,rms}$ the plot shows the mean and 95% confidence interval (defined as 1.96σ) of the $C_{p,rms}$ values obtained from all time series in each group. For calculation of $C'_{p,min}$, instead of subdividing the 10-min period in 16 windows, the absolute minima from each 10-min window in a group is taken to be an independent sample when performing the extreme value analysis described in Section 3.3. Missing datapoints are where a bin had insufficient data for the extreme value analysis. The plot confirms the above observations, and further highlights the dependency of the fluctuating pressure statistics. In particular, it appears that $C_{p,rms}$ depends quite strongly on the freestream turbulence intensity in the upstream separation region, while the dependency is reduced in the shear layer and wake forming around the cylinder further downstream.

To further investigate the influence of the incoming flow's turbulence on pressure statistics, we can isolate measurements in the windward separation and cylinder wake regions. As indicated by the dividing lines in Fig. 15, $[0, 45]°$ and $[315, 360]°$ is considered windward separation, while $[160, 200]°$ is leeward separation. Fig. 16 shows scatter plots of the $C_{p,rms}$ measurements as a function of the turbulence parameter η (see Section 3.3) for each of these regions. The plots also indicate linear fits to the data. In both flow regions, increased η results in more turbulent pressure measurements. However, the slope of the fit is more than twice as large in the windward separation region, indicating a greater sensitivity of $C_{p,rms}$ to η. In other words, I_u and $L_{u,x}$ have a lesser influence in the leeward wake compared with the windward side of the building.

4.3. Power spectra

Fig. 17 shows ensemble averaged spectra from measurements in the windward separation region and the cylinder wake region. Individual spectra were calculated for each 10-min period, followed by grouping them according to turbulence intensity bins and then ensemble averaging. For reference, the anemometer measures with a sampling frequency of 1 Hz, so its turbulence intensity only characterizes the timescales to the left of 0.5 Hz. For both locations, higher turbulence

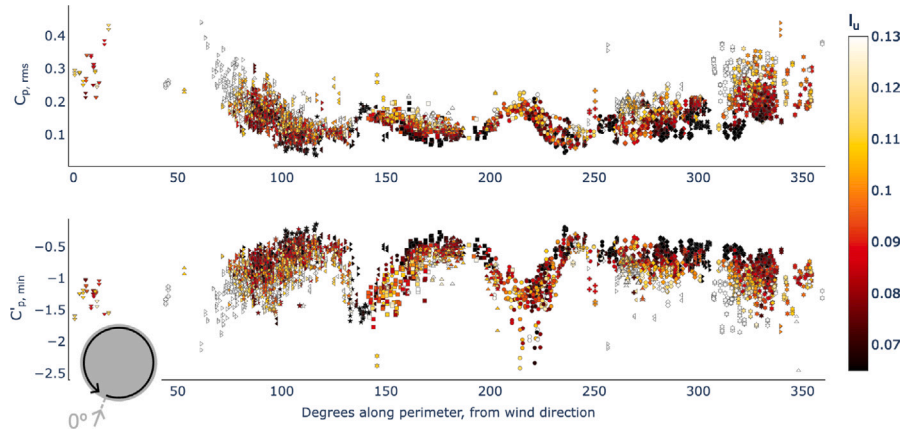

Fig. 14. $C_{p,rms}$ and $C'_{p,min}$ around the perimeter of the Space Needle's sloped roof. Marker color corresponds to turbulence intensity as measured by the rooftop anemometer and marker shape corresponds to the mote that took the measurement. The meaning of the x-axis is illustrated by the diagram at bottom left.

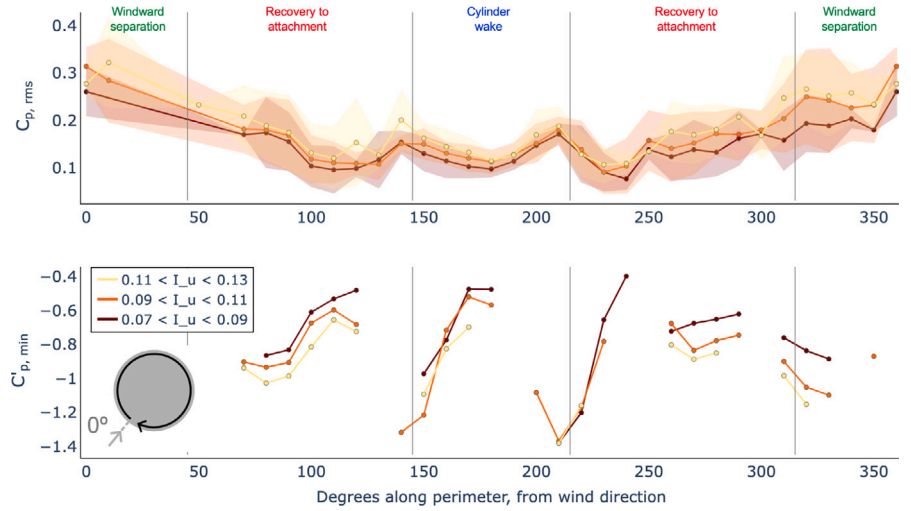

Fig. 15. $C_{p,rms}$ and $C'_{p,min}$ around the perimeter of the Space Needle's sloped roof, binned by position (10° bins) and turbulence intensity. The shaded regions in the $C_{p,rms}$ plot represent the 95% confidence interval, defined as 1.96σ.

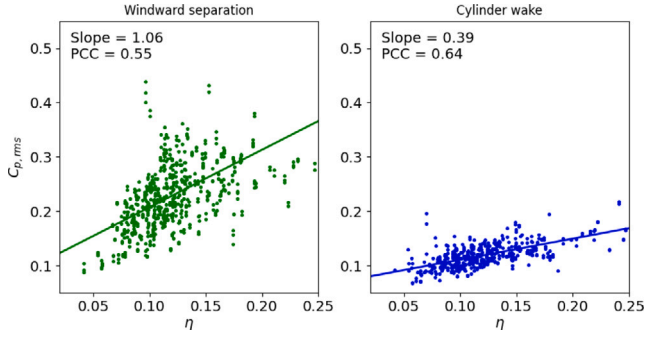

Fig. 16. $C_{p,rms}$ versus η for the alternate separation regions. The Pearson Correlation Coefficient (PCC) of the fit is annotated.

intensity measured by the anemometer results in increased spectral density in the fluctuating surface pressures. The increase occurs primarily at the larger scales: the curves of different turbulence intensities start to collapse on each other at a lower frequency. The increase is also more pronounced in the windward separation region compared to the cylinder wake region. The windward separation region has overall more energy content at the larger scales, indicating that the larger scales in the approach wind field break up due to the interaction of the flow with the building. The difference observed in the spectra is consistent with the findings of the previous subsection that inflow turbulence plays a dominant role for the windward region, but its influence is diminished on the leeward side in the secondary separation zone and the shear layers that originate from the raised central roof geometry.

4.4. Peak factor

Fig. 18 shows the peak factor magnitude $|g|$, calculated from each 10-min measurement period, around the building perimeter. The mean of each 10° position bin is also shown. No binning is done by measured turbulence intensity because of its correlation with $C_{p,rms}$ - i.e., dividing by the latter when calculating g removes the dependence. In most locations, the estimated peak factor exceeds the value of 3.4 used in ASCE 7–10, which is shown on the plot as a dashed line. The peak factor falls approximately within the range $4 < |g| < 7$ for most of the building perimeter, but the two shear layer regions on the leeward side see considerably higher values of $|g|$. For the 130° position, the maximum value over an individual 10-min window is as high as 14.6, while the mean value across all 10-min periods is 9.0. We note that the peak factor at this same position, calculated from the ensemble estimates for $C'_{p,min}$ and $C_{p,rms}$ (shown in Fig. 15), are very similar with values of 8.4, 9.0 and 9.3.

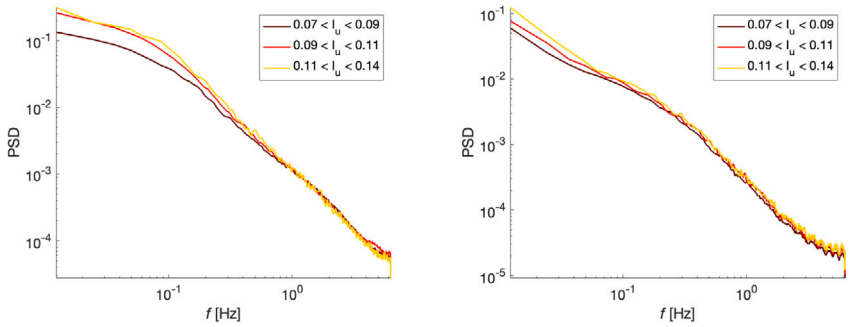

(a) Windward separation region, $[0, 45]^\circ \cup [315, 360]^\circ$.

(b) Cylinder wake region, $[160, 220]^\circ$.

Fig. 17. Ensemble averaged pressure spectra for measurements in the two separated flow regions.

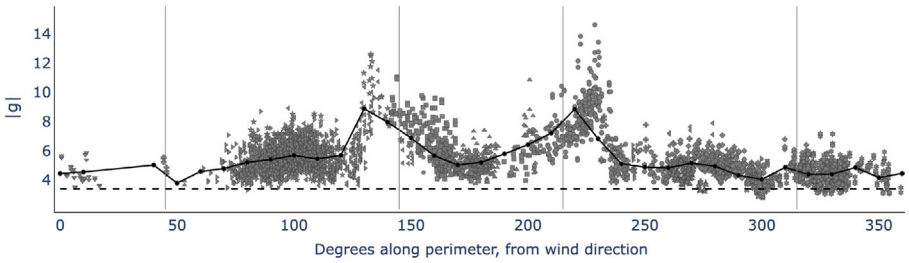

Fig. 18. Peak factor magnitude around the perimeter of the Space Needle's sloped roof, with mean for each 10° position bin.

4.5. Skewness and kurtosis of C_p' fluctuations

Skewness and kurtosis of the 10-min C_p' time series are plotted in Fig. 19. As with peak factor, no trend with the measured turbulence intensity was observed and so the coloring is not shown. The skewness plot shows that the fluctuation distributions of the two separation regions are highly skewed, but with opposite signs: the windward region of high $C_{p,rms}$ has positive skewnesses up to +2.4 while the leeward regions have negatively-skewed fluctuations, down to −2. In the kurtosis plot, the dashed line indicates a kurtosis of 3.5, which (Kumar and Stathopoulos, 2000) considers to be the threshold of non-Gaussianity. The high kurtosis values in both separation regions confirm that the pressure time series are strongly non-Gaussian.

The positive skewness in the windward region is noteworthy, since skewness is typically observed to be negative in separation regions. The positive values induce less negative minimum peak pressures, and lower values of the peak factor in the windward separation region compared to the shear layers adjacent to the cylinder wake (see Fig. 18). Analysis of individual pressure time series in this region indicates that the signal exhibits intermittent high positive fluctuations relative to the mean. We hypothesize that this positive skewness is induced by the flow intermittently impinging on the sloped windward side or the roof and will further investigate this result in future work that will leverage computational modeling.

Fig. 20 presents the same data as Fig. 20, but in the form of a scatter plot of kurtosis versus skewness. The color of the points corresponds to location on the sloped roof perimeter with the angle in the range [0,180]° as the two sides of the building have been collapsed on account of the symmetry. The gray area indicates C_p distributions with a skewness less than 0.5 and kurtosis less than 3.5, which can be considered to be Gaussian (Kumar and Stathopoulos, 2000). The figure confirms how frequent non-Gaussian pressure fluctuations are: only 43% of distributions fall inside the shaded region. Furthermore, most non-Gaussian distributions occur in regions of separation, as repeatedly noted in the literature. The dashed black line in Fig. 20 is the relationship expected for a log-normal distribution; the close adherence of datapoints to this line indicates the C_p' distributions can be reasonably well-modeled as being log-normal. A similar correlation between skewness and kurtosis has previously been identified from wind tunnel experiments on a high-rise building (Yang et al., 2022b) and on low-rise building roofs (Kumar and Stathopoulos, 2000), although those experiments only revealed regions with negative skewness.

Finally, we note that Yang et al. (2022b) identified a correlation between skewness and kurtosis and the turbulence length scale in the approach flow, but we could not identify a similar correlation from our field measurements. This result could indicate an actual absence of correlation for the specific combination of building geometry and approach flow characteristics considered here. However, it could also be a result of insufficient convergence of the skewness and kurtosis estimates calculated from the available 10-min time series. This possibility is evident from the wide spread of the kurtosis values calculated in the windward separation region and the leeward shear layers. A larger number of samples obtained under similar approach wind conditions (in terms of the length scales) might therefore be needed to obtain skewness and kurtosis estimates with an uncertainty that is lower than the expected correlation effect. The relationship between the distribution shape and the turbulence length scale will be further investigated using future computational analysis, where longer time series under quasi-steady approach wind conditions can be recorded.

5. Conclusions

A sensing network to unobtrusively measure wind pressure fluctuations on buildings was designed, and the potential of the network for gathering long-term data on a high-rise building was demonstrated. The network design involved the development of a custom data-logger that uses the Bosch Sensortec BMP388 absolute pressure sensor. With only 1.7 Pa RMS noise and low long-term drift, the sensor is able to measure pressure coefficients within ±0.1 at relatively low windspeeds ($U > 10$ m/s). The sensor's capability to accurately measure fluctuating pressure statistics was verified through a comparison with measurements obtained from a standard differential sensor in an atmospheric

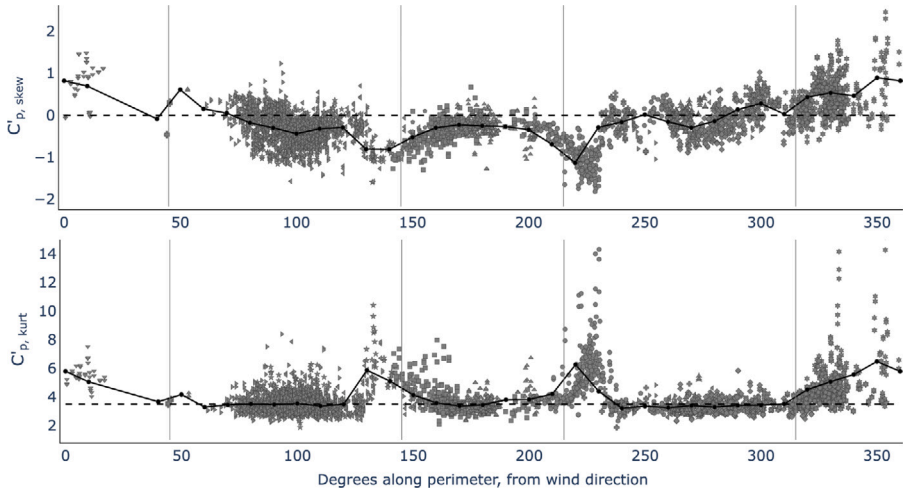

Fig. 19. Skewness (top) and kurtosis (bottom) of C_p' distributions for time series measured at locations around the perimeter of the Space Needle's sloped roof, with mean for each 10° position bin. Data point shape corresponds to mote.

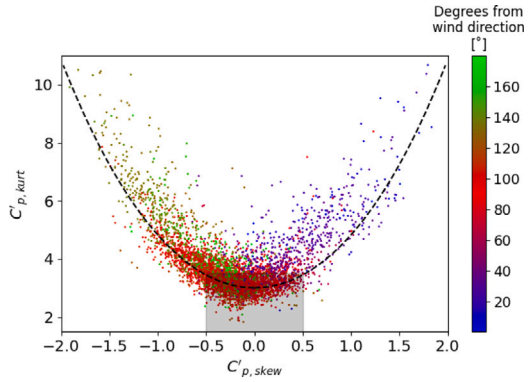

Fig. 20. Kurtosis versus skewness of C_p' distributions for time series measured at locations around the perimeter of the Space Needle's sloped roof.

boundary layer wind tunnel experiment. The comparison showed differences in fluctuation pressure coefficient statistics less than 0.1 between the two sensor types, confirming the ability to accurately measure turbulence statistics. The network motes are discreet, customizable, and weatherproof, and they are also lower-cost than any commercially available alternatives: each mote costs only between $200 and $300 in materials. The data-logger will work with almost any I2C or SPI sensor, such that it can be used for a wide range of environmental sensing applications.

To demonstrate the potential of the pressure sensing network, we obtained over 1000 h of time series data at 10 positions along the perimeter of the sloped roof of the Space Needle, a 184 m tall observation tower. Statistics of the fluctuating pressures, $C_{p,rms}$, $C'_{p,min}$, and peak factor, as well as skewness and kurtosis were calculated based on the time series. The measurements indicate two separation regions. On the windward side, the flow separates at the glass wall around the observation deck. On the leeward side, flow separation is induced by the cylindrical extrusion that supports the upper deck. In both regions, $C_{p,rms}$ and $C'_{p,min}$ were found to depend on the freestream turbulence intensity and length scale, but the dependency is strongest on the windward side. The pressure fluctuation distributions in both regions were observed to be non-Gaussian, with positive skewness in the windward separation region, and negative skewness in the leeward separation region. The most severe peak pressures occur near the edge of the leeward separation region, where the peak factor was found to be up to 2.6 times larger than the value of 3.4 used in the North American building code.

The measurements presented in this paper demonstrate how full-scale measurements performed over long time periods can provide significant insight into full-scale wind pressures and their dependence on the approach wind characteristics. In future work we intend to combine the measurements with large-eddy simulations for validation of the numerical models and for further analysis of the flow physics that produce the observed pressure time series. We also envision future measurement campaigns combining the deployment of the pressure sensors with more extensive measurements of the turbulence in the incoming wind field, for example using LiDAR profilers. While such measurement campaigns will be costly, the results presented in this paper indicate that combined measurements of the approach wind and the resulting pressure field offer unprecedented potential for improving our understanding of peak wind loading.

CRediT authorship contribution statement

John Hochschild: Writing – original draft, Methodology, Investigation, Conceptualization. **Catherine Gorlé:** Writing – review & editing, Supervision, Conceptualization.

Declaration of competing interest

The authors declare that they have no known competing financial interests or personal relationships that could have appeared to influence the work reported in this paper.

Data availability

The data is shared via Mendeley and is linked in the manuscript.

Acknowledgments

This material is based upon work supported by the National Science Foundation, United States of America under Grant No. (1749610). Any opinions, findings, and conclusions or recommendations expressed in this material are those of the author(s) and do not necessarily reflect the views of the National Science Foundation. Additional support was obtained through an ARUP Global Research Challenge award, and the Stanford Leavell fellowship program. We are grateful to Melissa Burton and Rubina Ramponi from ARUP for their early guidance on the design of the sensor network. We also extend our gratitude to David Wright for making the Space Needle available for this research work and to Joel Dazey and other Space Needle staff for their support of the project.

References

American Society of Civil Engineers, 2022. Minimum Design Loads and Associated Criteria for Buildings and Other Structures. American Society of Civil Engineers.

Bosch Sensortec, 2018. BMP388: Digital pressure sensor. Rev. 1.1.

Cao, Yong, Tamura, Tetsuro, Kawai, Hidenori, 2019. Investigation of wall pressures and surface flow patterns on a wall-mounted square cylinder using very high-resolution cartesian mesh. J. Wind Eng. Ind. Aerodyn. 188, 1–18.

Chen, Stefanos, 2021. The downside to life in a supertall tower: Leaks, creaks, breaks. N.Y. Times.

Cochran, L.S., Cermak, J.E., 1992. Full- and model-scale cladding pressures on the texas tech university experimental building. J. Wind Eng. Ind. Aerodyn. 43 (1), 1589–1600, International Conference on Wind Engineering.

Cook, N.J., Mayne, J.R., 1979. A novel working approach to the assessment of wind loads for equivalent static design. J. Wind Eng. Ind. Aerodyn. 4 (2), 149–164.

Cook, N.J., Mayne, J.R., 1980. A refined working approach to the assessment of wind loads for equivalent static design. J. Wind Eng. Ind. Aerodyn. 6 (1–2), 125–137.

Dalgliesh, W. Alan, 1971. Statistical treatment of peak gusts on cladding. J. Struct. Div. 97 (9), 2173–2187.

Dalgliesh, William Alan, Templin, J.T., Cooper, Kevin Russell, 1980. Comparisons of wind tunnel and full-scale building surface pressures with emphasis on peaks. In: Wind Engineering. Elsevier, pp. 553–565.

Hagos, A., Filmon, H., Chowdhury, A.G., Yeo, D., 2014. Comparisons of two wind tunnel pressure databases and partial validation against full-scale measurements. J. Struct. Eng. 140 (10), 04014065.

Ho, T.C.E., Surry, D., Morrish, D., 2003. Nist/ttu cooperative agreement/windstorm mitigation initiative: wind tunnel experiments on generic low buildings. Technical report, Western University.

Kasperski, M., 2003. Specification of the design wind load based on wind tunnel experiments. J. Wind Eng. Ind. Aerodyn. 91 (4), 527–541.

Kumar, K. Suresh, Stathopoulos, T., 2000. Wind loads on low building roofs: a stochastic perspective. J. Struct. Eng. 126 (8), 944–956.

Lamberti, Giacomo, Gorlé, Catherine, 2020. Sensitivity of LES predictions of wind loading on a high-rise building to the inflow boundary condition. J. Wind Eng. Ind. Aerodyn. 206, 104370.

Liao, Yizheng, Mollineaux, Mark, Hsu, Richard, Bartlett, Rebekah, Singla, Anubhav, Raja, Adnan, Bajwa, Ravneet, Rajagopal, Ram, 2014. Snowfort: An open source wireless sensor network for data analytics in infrastructure and environmental monitoring. IEEE Sens. J. 14 (12), 4253–4263.

Liu, Min, Chen, Xinzhong, Yang, Qingshan, 2017. Estimation of peak factor of non-Gaussian wind pressures by improved moment-based Hermite model. J. Eng. Mech. 143 (7), 06017006.

Liu, Z., Prevatt, D.O., Aponte-Bermudez, L.D., Gurley, K.R., Reinhold, T.A., Akins, R.E., 2009. Field measurement and wind tunnel simulation of hurricane wind loads on a single family dwelling. Eng. Struct. 31 (10), 2265–2274.

Morrison, Murray J., Brown, Tanya M., Liu, Zhuzhao, 2013. Comparison of field and full-scale laboratory peak pressures at the IBHS research center. In: Advances in Hurricane Engineering: Learning from Our Past. pp. 1109–1124.

Okada, H., Ha, Y.-C., 1992. Comparison of wind tunnel and full-scale pressure measurement tests on the texas texh building. J. Wind Eng. Ind. Aerodyn. 43 (1), 1601–1612, International Conference on Wind Engineering.

Peng, X., Yang, L., Gavanski, E., Gurley, K., Prevatt, D., 2014. A comparison of methods to estimate peak wind loads on buildings. J. Wind Eng. Ind. Aerodyn. 126, 11–23.

Pomaranzi, Giulia, Amerio, Luca, Schito, Paolo, Lamberti, Giacomo, Gorlé, Catherine, Zasso, Alberto, 2022. Wind tunnel pressure data analysis for peak cladding load estimation on a high-rise building. J. Wind Eng. Ind. Aerodyn. 220, 104855.

Ricci, M., Patruno, L., De Miranda, S., 2017. Wind loads and structural response: Benchmarking LES on a low-rise building. Eng. Struct. 144, 26–42.

Ricci, M., Patruno, L., Kalkman, I., De Miranda, S., Blocken, B., 2018. Towards LES as a design tool: Wind loads assessment on a high-rise building. J. Wind Eng. Ind. Aerodyn. 180, 1–18.

Richardson, G.M., Hoxey, R.P., Robertson, A.P., Short, J.L., 1997. The silsoe structures building: Comparisons of pressures measured at full scale and in two wind tunnels. J. Wind Eng. Ind. Aerodyn. 72, 187–197.

Richardson, G.M., Surry, D., 1991. Comparisons of wind-tunnel and full-scale surface pressure measurements on low-rise pitched-roof buildings. J. Wind Eng. Ind. Aerodyn. 38, 249–256.

Saathoff, Patrick J., Melbourne, William H., 1997. Effects of free-stream turbulence on surface pressure fluctuations in a separation bubble. J. Fluid Mech. 337, 1–24.

Sridhar, S., Pineli, J.-P., Zhang, J., Subramanian, C.S., Wang, J., Sun, J., Lazarus, S., Besing, H., 2021. Wireless sensor network system data acquisition and analysis using DesignSafe-CI.

Subramanian, Chelakara, Lapilli, Gabriel, Kreit, Frederic, Pinelli, Jean-Paul, Kostanic, Ivica, 2011. Experimental and computational performance analysis of a multi-sensor wireless network system for hurricane monitoring. Sensors Transduce. 10, 206.

Subramanian, Chelakara, Pinelli, Jean-Paul, Kostanic, Ivica, Lapilli, Gabriel, 2012. Design, development and testing of a wireless multi-sensor network system. J. Mech. Eng. Automat. 2, 169–183.

Tieleman, H.W., 2003. Wind tunnel simulation of wind loading on low-rise structures: A review. J. Wind Eng. Ind. Aerodyn. 91, 1627–1649.

Vargiemezis, Themistoklis, Gorlé, Catherine, 2024. Comparison of LES and wind tunnel tests of wind loads on an isolated low-rise building. J. Wind Eng. Ind. Aerodyn..

Wacker, J., Friedrich, R., Plate, E.J., Bergdolt, U., 1991. Fluctuating wind load on cladding elements and roof pavers. J. Wind Eng. Ind. Aerodyn. 38 (2–3), 405–418.

Yang, Xiongwei, Du, Shubi, Li, Mingshui, Qin, Chuan, Zhang, Haicheng, Yu, Jianhan, 2022a. Effects of the turbulence integral scale on the non-Gaussian properties and extreme wind loads of surface pressure on a CAARC model. J. Struct. Eng. 148 (11), 04022174.

Yang, X., Du, S., Li, M., Qin, C., Zhang, H., Yu, J., 2022b. Effects of the turbulence integral scale on the non-Gaussian properties and extreme wind loads of surface pressure on a CAARC model. J. Struct. Eng. 148 (11), 04022174.